Earth and Space Science

TECHNICAL REPORTS: METHODS
10.1029/2019EA000817

New Technique to Retrieve Tropospheric Temperature Using Vibrational and Rotational Raman Backscattering

Jia Su[1], M. Patrick McCormick[1], and Liqiao Lei[1,2]

[1]Center for Atmospheric Sciences, Department of Atmospheric and Planetary Sciences, Hampton University, Hampton, VA, USA, [2]NASA Langley Research Center, Hampton, VA, USA

Key Points:

- A new technique is proposed to retrieve tropospheric temperature profile using vibrational and rotational Raman backscattering
- The new technique can decrease retrieval errors caused by insufficient suppression of the Mie backscattering in the rotational Raman detection channels
- The new technique is validated by showing the good agreements between HU lidar and radiosonde measurements of temperature

Correspondence to:
J. Su,
jia.su@hamptonu.edu

Citation:
Su, J., McCormick, M. P., & Lei, L. (2020). New Technique to Retrieve Tropospheric Temperature Using Vibrational and Rotational Raman Backscattering. *Earth and Space Science*, *7*, e2019EA000817. https://doi.org/10.1029/2019EA000817

Received 5 AUG 2019
Accepted 21 DEC 2019
Accepted article online 2 JAN 2020

©2020. The Authors.
This is an open access article under the terms of the Creative Commons Attribution License, which permits use, distribution and reproduction in any medium, provided the original work is properly cited.

Abstract A new technique is advanced to obtain tropospheric temperature profile using vibrational Raman (VR) and rotational Raman (RR) backscattering. The proposed technique can obtain tropospheric temperature and decrease retrieval errors caused by insufficient suppression of the Mie backscattering in the RR detection channels. The retrieval equations are obtained using VR and RR lidar equations. The feasibility of this technique is demonstrated by applying the algorithm to the Hampton University VR and RR lidar signals. Intercomparisons of these atmospheric temperature retrievals from the Hampton University lidar show good agreement with local radiosonde measurements. Moreover, the proposed technique is applied to a cloudy case and is further validated by showing the good agreements with radiosonde measurements of cloud temperature.

1. Introducti on

Temperature is a key parameter to monitor global warming and plays an important role in climatology, meteorology, atmospheric dynamics, and chemistry. Recently, attention has been brought to the recorded tropospheric temperature around the start of the 21st century, which has been slower than the rate calculated using climate models [Santer et al., 2017). Long-term observations of tropospheric temperature profiles are very crucial for numerical weather prediction, investigating many atmospheric processes and climate monitoring (Newsom et al., 2013). Moreover, the tropospheric temperature profile is necessary as an initial input to many remote sensing instruments including lidars and satellites to determine other quantities [Ansmann et al., 1992; Sherlock et al., 1999; Behrendt & Reichardt, 2000]. Measurements of the intensity of infrared radiation from the ground or from a satellite are usually used to retrieve the temperature [Aumann & Chahine, 1976; Cooper, 1988]. These instruments generally can provide accurate temperature profiles and other variable profiles. However, their operation can be expensive and labor. Thus, most operational sites around the world only launch radiosondes on a twice-daily basis, resulting in temporally under sampled observations, particularly in the lower troposphere (Su et al., 2013). Remote sensing techniques offer the potential for autonomous operation and improved temporal resolution.

Rotational Raman (RR) lidars have been proven to be a very useful remote sensing tool to measure tropospheric temperature at the present (Arshinov et al., 1983; Cooney, 1972; Su et al., 2008; Vaughan et al., 1993). The major technical challenge for temperature measurements with the RR technique is to achieve sufficient suppression ($>10^{-7}$) of the elastic backscatter signal in the two RR channels (low-J and high-J RR channels, J is quantum number). The problem is particularly serious in the low-J RR channel because of its close proximity (<0.5 nm at $\lambda = 354.7$ nm). Generally, conventional RR lidars use two narrow-band interference filters to block the elastic-scattering signal in the low-J RR channel and one narrow-band interference filter in the high-J RR channel and this has been well verified under the clear sky [Arshinov et al., 1983; Vaughan et al., 1993]. However, this will become an issue when there is the thick aerosol layer or cloud along output laser beam path. Because the thick aerosol layer or cloud elastic backscattering is very strong and low-J RR-wavelength is so close to the elastic-scattering wavelength, the narrow-band interference filter in the low-J RR-channel cannot completely suppress the elastic backscattering, which makes it impossible to retrieve temperature without any correction (Su et al., 2013). Herein, we proposed a new technique to retrieve tropospheric temperature profile using one vibrational Raman (VR) backscattering and one high-J RR backscattering. The proposed technique can obtain tropospheric temperature and decrease retrieval errors caused insufficient suppression of the elastic backscattering in the low-J RR detection channel. The

retrieval equations are obtained using VR and RR lidar signals. Tropospheric temperature was obtained by applying the proposed technique to the Hampton University (HU) lidar VR and RR signals. This technique is further validated by showing the good agreements between HU lidar and radiosonde measurements of temperature.

2. Method

RR and VR lidar equations are expressed as [Cooney et al., 1972; Ansmann et al., 1990; Whiteman et al., 1992]

$$X_{vr}(\lambda_{vr},Z)=C_{vr}\frac{N(Z)\sigma(\lambda_{vr})}{Z^2}e^{-\int_0^Z\left[\alpha_m\left(\lambda_i,z'\right)+\alpha_a\left(\lambda_i,z'\right)+\alpha_m\left(\lambda_{vr},z'\right)+\alpha_a\left(\lambda_{vr},z'\right)\right]dz'} \tag{1}$$

$$X_{rr}(\lambda_{rr},Z)=C_{rr}\frac{N(Z)v_J^4g_J(J)\frac{Bhc}{KT(Z)}(2J+1)e^{-\frac{Bhc}{KT(Z)}J(J+1)}\left|H_J^J\right|^2}{Z^2}e^{-\int_0^Z\left[\alpha_m\left(\lambda_i,z'\right)+\alpha_a\left(\lambda_i,z'\right)+\alpha_m\left(\lambda_{rr},z'\right)+\alpha_a\left(\lambda_{rr},z'\right)\right]dz'} \tag{2}$$

where in equations (1) and (2) X_{vr} and X_{rr} are RR and VR lidar signals; λ_{vr}, λ_{rr}, and λ_i refer to wavelengths of VR and RR and incident wavelength; Z is altitude; C_{rr} and C_{vr} are RR and VR lidar constants; N is number density of nitrogen molecules; $\sigma(\lambda_{vr})$ is nitrogen VR backscattering cross section; α_m and α_a refer to extinction coefficients of molecule and aerosol; v_J is RR frequency shift; $g_J(J)$ is the statistical weight factor of the pure rotational line due to a nuclear spin; J is quantum number; B is rotational constant; c is light speed; h is Planck constant; K is the Boltzmann constant; T is temperature; $\left|H_J^J\right|^2$ is squared matrix elements of the corresponding rotational transition.

The ratio of VR lidar signal to RR lidar signal is expressed as

$$\frac{X_{vr}(\lambda_{vr},Z)}{X_{rr}(\lambda_{rr},Z)}=A\frac{T(Z)}{e^{\frac{D}{T(Z)}}}\Delta T_a\Delta T_m \tag{3}$$

$$A=\frac{C_{vr}\sigma(\lambda_{vr})}{C_{rr}v_J^4g_J(J)\frac{Bhc}{K}(2J+1)\left|H_J^J\right|^2}$$

$$\mathrm{D}=-\frac{\mathrm{Bhc}}{\mathrm{K}}\mathrm{J(J+1)}$$

$$\Delta T_a=e^{-\int_0^Z\left[\alpha_a\left(\lambda_{vr},z'\right)-\alpha_a\left(\lambda_{rr},z'\right)\right]dz'}$$

$$\Delta T_m=e^{-\int_0^Z\left[\alpha_m\left(\lambda_{vr},z'\right)-\alpha_m\left(\lambda_{rr},z'\right)\right]dz'}$$

where A and D are calibrated coefficients which can be obtained using balloon sounding's temperature; ΔT_α is aerosol transmission ratio of RR to VR and can be obtained using aerosol extinction retrieved from VR lidar signal (Ansmann et al., 1990). ΔT_m is molecular transmission ratio of RR to VR and can be obtained using atmospheric model.

The tropospheric temperature can be obtained from equation (4).

$$|P[T(Z)]|=\left|\frac{X^m{}_{vr}(\lambda_{vr},Z)}{X^m{}_{rr}(\lambda_{rr},Z)}-A\frac{T(Z)}{e^{\frac{D}{T(Z)}}}\Delta T_a\Delta T_m\right| \tag{4}$$

where $X^m{}_{vr}(\lambda_{vr}, Z)$ and $X^m{}_{rr}(\lambda_{rr}, Z)$ are measured VR and RR lidar signals. Trial values of $T(Z)$ (from 160 to 330 k with an increment of 0.1 k) are applied to equation (4). For each trial value of $T(Z)$, an absolute value of $P[T(Z)]$ is calculated. Thus, $T(Z)$ is determined when the absolute value of $P[T(Z)]$ is minimized.

3. HU Lidar System

The existing HU Raman-Mie lidar system shown in Figure 1 currently consists of a zenith-viewing Nd:YAG laser, which emits three fixed laser wavelengths (1,064, 532, and 355 nm), a 48-in. noncoaxial Cassegrain telescope receiver with adjustable 1- to 4-mrad field-of-view, an optical separation system built with beam

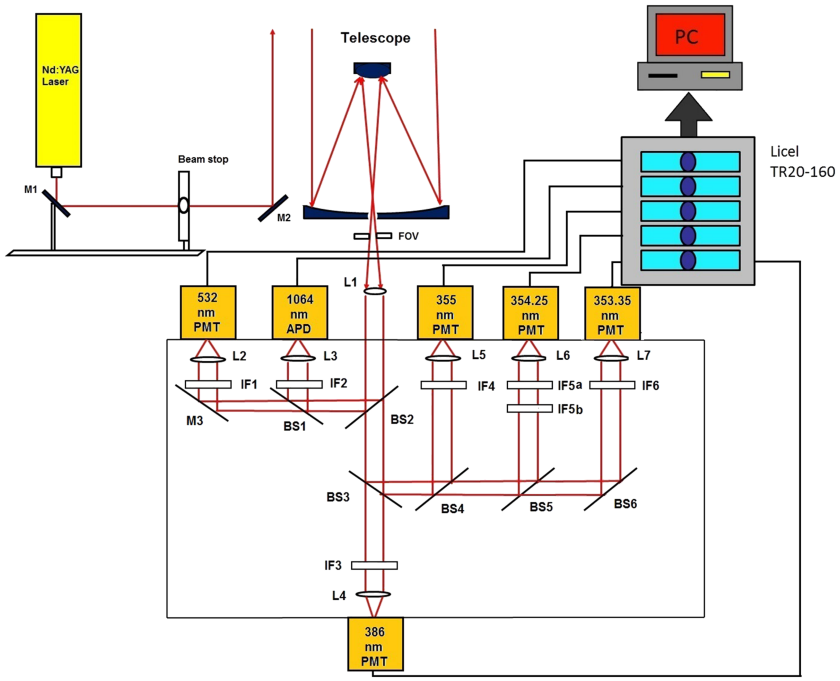

Figure 1. HU lidar system (L = lens, M = mirror, BS = beamsplitter, IF = interference filter, FOV = field of view, PMT = photomultiplier tube, APD = avalanche photodetector).

splitters and interference filters, detecting system including photomultiplier tube and avalanche photodiode, and a Licel optical transient recorder data reduction system. Table 1 shows the specifications of HU lidar system. The lidar can be configured to measure elastic backscattering from aerosols and clouds at the three laser output wavelengths, and at the same time measure VR and RR backscatterings excited by the 355-nm laser third harmonic output with high resolution (7.5 m). The detecting return signals of HU lidar are between the ranges of 1.5 km and approximately 30 km. Two lidar elastic signals (355 and 532 nm), two RR backscattered signals (353.35 and 354.2 nm), and one VR backscattered signal (386 nm) are received by five photomultiplier tubes, while one lidar elastic signal (1,064 nm) is received by an avalanche photodiode. This provides the ability for HU lidar to measure aerosol backscatter and extinction coefficients from the elastic signals, and temperature, lidar ratios, and optical depth from the VR and RR signals, respectively, with a vertical range that extends from the near surface to the top of the troposphere depending on atmospheric conditions. Figure 1 also shows the structure and optical separation system of HU lidar. And Table 2 shows the parameters of HU lidar filters.

Table 1
HU Lidar Specifications

Receiver: 48-in. Cassegrainian telescope	
Type	Noncoaxial
Diameter (in.)	48
Focal length (mm)	480
Field of view (mrad)	1–4
Detectors	Hamamatsu R7400U-02 Photomultiplier Tube
	Perkin & Elmer C30956E-TC Avalanche Photodiode
Laser: Continuum Powerlite 8020 Nd:YAG	
Wavelength (nm)	1,064, 532, 355, and 266
Repetition rate (Hz)	20
Energy (mJ)	1064 nm: 1200
	532 nm: 550
	355 nm: 300
Beam divergence (mrad)	0.5
Linewidth (cm^{-1})	1
Data acquisition: LICEL Optical Transient Recorder TR20-160	
Analog acquisition	12 bit A/D resolution
	20-MHz sampling rate
Photon counting acquisition	250-MHz maximum counting rate
Typical minimum height resolution	15 m

4. Results

This new technique has been applied to the HU lidar measurements, and a case on a clear night is presented in Figure 2. HU lidar elastic (black line), VR (blue line), and RR (red line) signals measured at 20:00 on 5 March 2019 are shown in Figure 2a. The average time for these signals is 15 min. Aerosol extinction coefficients at 355 nm are retrieved using Raman technique shown in Figure 2b. There are some aerosol layers in the sky. Figure 2c present vertical profiles of temperature obtained using proposed technique and conventional

Table 2
The Parameters of HU Lidar Filters

Items	Description (all made by Materion corporation)
IF1	CWL: 532.0 ± 0.2 nm, FWHM: 1 ± 0.1 nm Peak Transmission > 40% *Blocking: 10^{-6} at 354.7 nm and 1064 nm 10^{-5} at all other points from 200–1,200 nm
IF2	CWL: 1064.0 ± 0.2 nm, FWHM: 1 ± 0.1 nm Peak transmission > 40% *Blocking: 10^{-6} at 354.7 nm and 532 nm 10^{-5} at all other points from 200–1200 nm
IF3	CWL: 386.68 ± 0.04 nm, FWHM: 0.3 ± 0.06 nm Peak transmission > 40% *Blocking: 10^{-6} at 354.7, 532, and 1,064 nm 10^{-5} at all other points from 200–1,200 nm
IF4	CWL: 354.7 ± 0.1 nm, FWHM: 1 ± 0.1 nm Peak transmission > 40% *Blocking: 10^{-6} at 532 and 532 nm 10^{-5} at all other points from 200–1,200 nm
IF5a, IF5b	CWL: 354.20 ± 0.04 nm, FWHM: 0.3 ± 0.06 nm Peak transmission > 40% *Blocking: 10^{-6} at 354.7, 532, and 1,064 nm 10^{-5} at all other points from 200–1,200 nm
IF6	CWL: 353.25 ± 0.04 nm, FWHM: 0.3 ± 0.1 nm Peak Transmission > 40% *Blocking: 10^{-6} at 354.7, 532, and 1,064 10^{-5} at all other points from 200–1,200 nm

RR technique from HU lidar. The temperature profile measured by the radiosonde at the same time is also presented in Figure 2c. The radiosonde is launched form HU campus (the distance between HU lidar and radiosonde launching site is about 10 m). The retrieved temperature results using the proposed technique agree well with results of RR technique and radiosonde. The statistical temperature uncertainty from the temperature profile received using the proposed technique is also presented in Figure 2c. Figure 2d shows temperature difference between the proposed technique and the local radiosonde. The temperature difference between the proposed technique and the local radiosonde is less than 3 k below 22 km. It proves that the proposed technique can well retrieve tropospheric temperature. To demonstrate the advantage of the proposed technique, a case on a cloudy night is presented in Figure 3. HU lidar elastic (black line), VR (blue line), and RR (red line) signals measured at 04:30 on 20 September 2018 are shown in Figure 3a. The average time for these signals is 15 min. A cloud layer between 4.5 and 5.2 km can be found from lidar elastic signal. Aerosol extinction coefficients at 355 nm are retrieved using Raman technique shown in Figure 3b. Figure 3c presents vertical profile of temperature obtained using proposed technique from HU lidar. The temperature profile measured by the radiosonde at the same time is also presented in Figure 3c. The retrieved cloud temperature outlined by a black dashed square using the proposed technique agrees well with radiosonde's. Figure 3d shows temperature difference between the proposed technique and the local radiosonde. The cloud temperature difference between the proposed technique and the local radiosonde is less than 1.5 K.

The temporal variation of HU-lidar-measured temperature using proposed technique between 19:30 on 5 March and 05:30 on 6 March 2019 is shown in Figure 4a. After sunset on 5 March, tropospheric temperature decreased due to surface cooling. However, the temperature decrease trend was disrupted at 23:30 on 5 March. After 23:30 on 5 March, the temperature increased in intensity and reached peak at 00:30 on 6 March. After 00:30 on 6 March, the temperature decrease trend was continued. To explain the disruption of temperature decrease trend, the temporal variation of corresponding range-corrected lidar signals at 532 nm was presented in Figure 4b. It was found that the boundary layer aerosol increased after 21:30 caused by night low-level jets at HU campus. HU campus is adjacent to the confluence of the Chesapeake Bay and

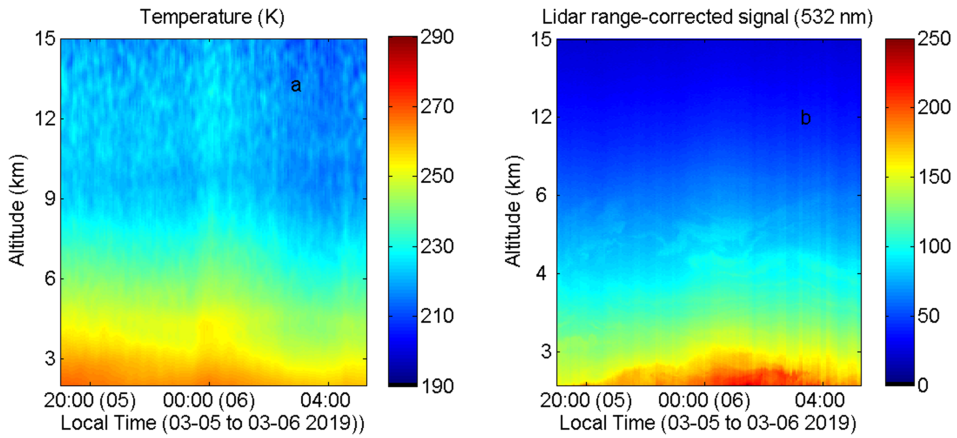

Figure 2. (a) HU lidar elastic (black),VR (blue line), and RR (red line) lidar signals; (b) aerosol extinction coefficients at 355 nm calculated using Raman technique; (c) temperature profiles obtained using the proposed technique (blue line), RR technique (black line) and radiosonde (red line); (d) temperature difference between the proposed technique and the local radiosonde launched in HU at 20:00 on 5 March 2019.

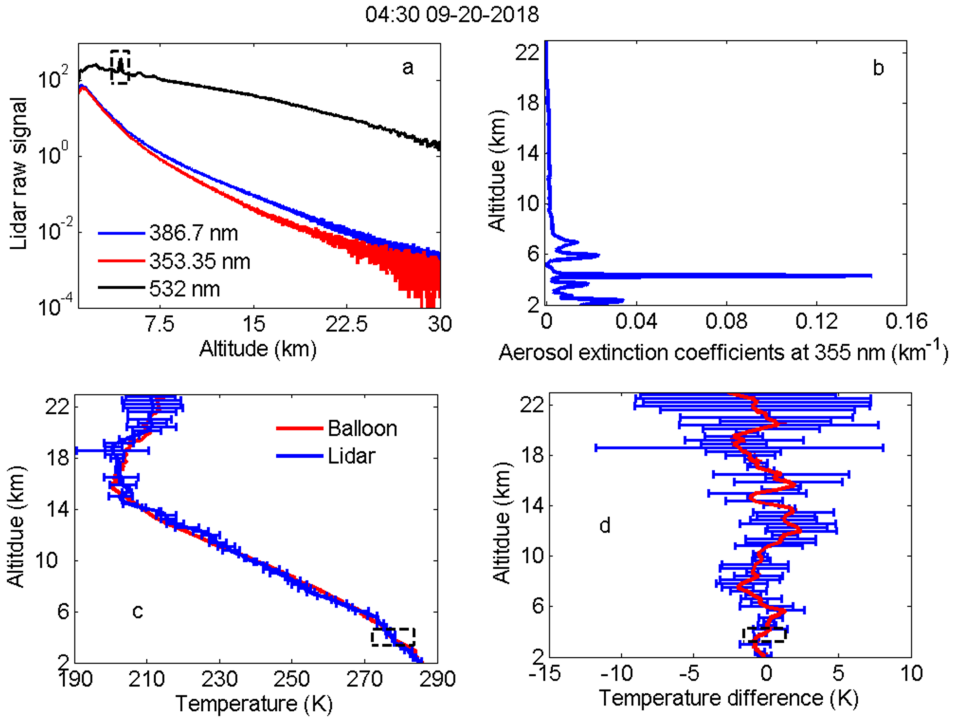

Figure 3. (a) HU lidar elastic (black),VR (blue line), and RR (red line) lidar signals; (b) aerosol extinction coefficients at 355 nm calculated using Raman technique; (c) temperature profiles obtained using the proposed technique (blue line) and radiosonde (red line); (d) temperature difference between the proposed technique and the local radiosonde launched in HU at 04:30 on 20 September 2018.

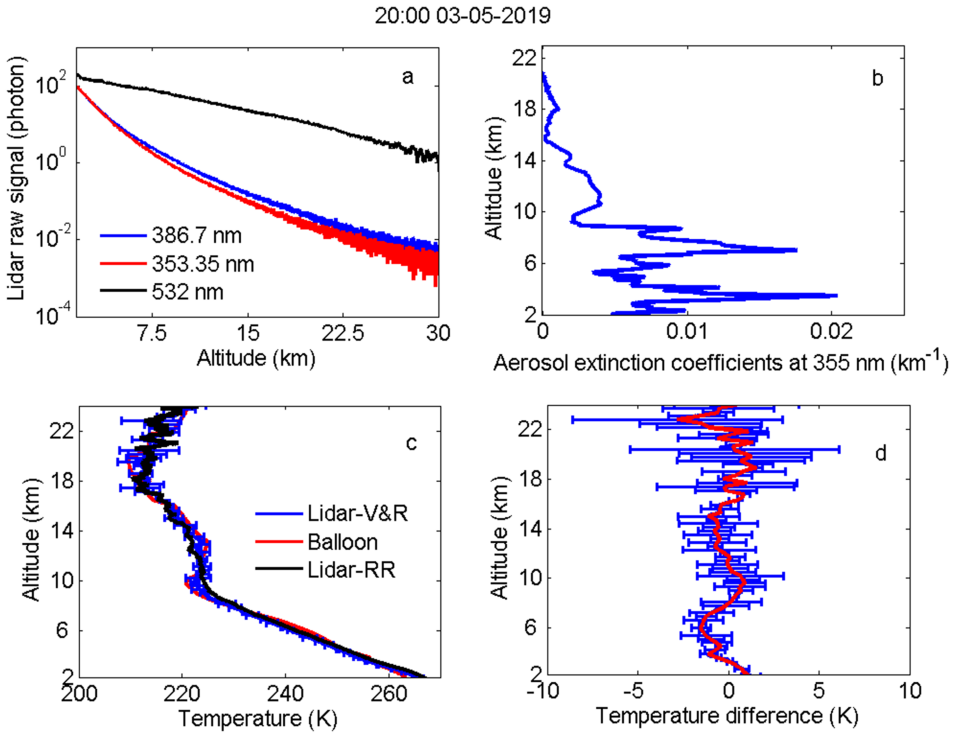

Figure 4. The temporal variation of HU-lidar-measured temperature using proposed technique (a) and 532-nm lidar range-corrected signal (b) between 19:30 on 0 March and 05:30 on 6 March 2019.

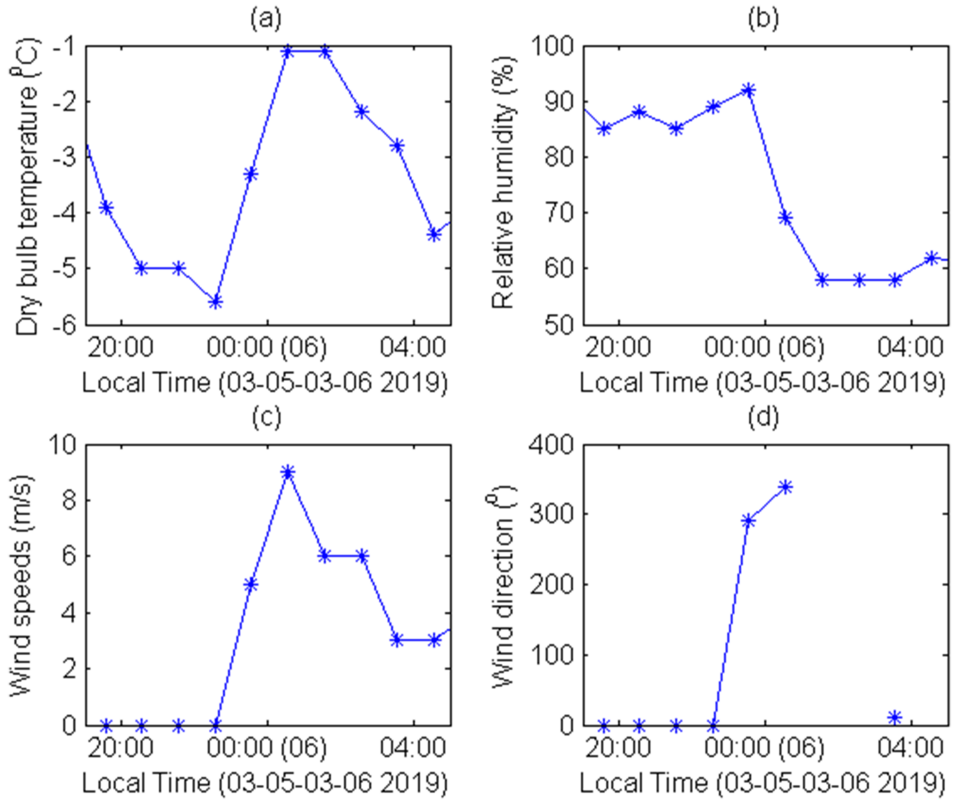

Figure 5. The nearby weather station ground observation: (a) dry bulb temperature, (b) relative humidity, (c) wind speed, and (d) wind direction.

the Atlantic Ocean where LLJs often form in the boundary layer during the spring and summer [Su et al., 2016]. Moreover, the nearby weather station (HAMPTON ROADS EXECUTIVE AIRPORT station) ground observation was shown in Figure 5. The ground weather information included dry bulb temperature, relative humidity, wind speeds, and wind direction. In Figure 5b, the ground wind speeds increased from about 23:00 and reached a peak at about 00:30 on 6 March. It proved that a low-level jet passed by Hampton road region. In Figure 5a, ground dry bulb temperature increased from about 23:00 and it agreed with HU lidar' results using the proposed technique. Also, it proved that the warm air passed by Hampton road region. So the disruption of temperature decrease trend was caused by night low-level jets, which brought much warm and moisture air to HU.

5. Conclusion

In conclusion, we described a lidar retrieval method that uses using one VR channel and one high-J RR signals to simultaneously determine the tropospheric temperature. The proposed technique can decrease retrieval errors caused insufficient suppression of the elastic-scattering signal in the low-J RR detection channel. The retrieval equations are obtained using VR and RR lidar equations. Tropospheric temperature was obtained by applying the proposed technique to HU lidar VR and RR signals. This technique is further validated by showing the good agreements between HU lidar and radiosonde measurements of temperature.

Acknowledgments
This study was supported by the PIRT project funded by the U.S. Army Research, Development and Engineering Command (AQC) Center (DOD) under HU PIRT Award 551150-211150) and the National Oceanic and Atmospheric Administration-Cooperative Science Center for Earth System and Sciences and Remote Sensing Technologies (NOAA-CESSRST) under the Cooperative Agreement Grant NA16SEC4810008. HU lidar data are available online (http://cas.hamptonu.edu/data-products/).

References

Ansmann, A., Riebesell, M., & Weitkamp, C. (1990). Measurement of atmospheric aerosol extinction profiles with a Raman lidar. *Optics Letters*, *15*, 746–751.

Ansmann, A., Wandinger, U., & Riebesell, M. (1992). Independent measurement of extinction and backscatter profiles in cirrus clouds by using a combined Raman elastic-backscatter lidar. *Applied Optics*, *31*, 7113.

Arshinov, Y. F., Bobrovnikov, S. M., Zuev, V. E., & Mitev, V. M. (1983). Atmospheric temperature measurements using a pure RR lidar. *Applied Optics*, *22*, 2984–2990.

Aumann, H. H., & Chahine, M. T. (1976). Infrared multidetector spectrometer for remote sensing of temperature profiles in the presence of clouds. *Applied Optics*, *15*, 2091–2096.

Behrendt, A., & Reichardt, J. (2000). Atmospheric temperature profiling in the presence of clouds with a pure RR lidar by use of an interference-filter-based polychromator. *Applied Optics*, *39*, 1372–1376.

Cooney, J. (1972). Measurement of atmospheric temperature profiles by Raman backscatter. *Journal of Applied Meteorology*, *11*, 108–112.

Cooper, W. A. (1988). Effects of coincidence on measurements with a forward scattering spectrometer probe. *Journal of Atmospheric and Oceanic Technology*, *5*, 823–826.

Newsom, R. K., Turner, D. D., & Goldsmith, J. E. M. (2013). Long-term evaluation of temperature profiles measured by an operational Raman lidar. *Journal of Atmospheric and Oceanic Technology*, *30*(8), 1616–1634.

Santer, B. D., Fyfe, J. C., Pallotta, G., Flato, G. M., Meehl, G. A., England, M. H., et al. (2017). Causes of differences in model and satellite tropospheric warming rates. *Nature Geoscience*, *10*(7), 478–485. https://doi.org/10.1038/ngeo2973

Sherlock, V., Hauchecorne, A., & Lenoble, J. (1999). Methodology for the independent calibration of Raman water-vapor lidar systems. *Applied Optics*, *38*, 5816.

Su, J., Felton, M., Lei, L., McCormick, M. P., Delgado, R., & Pé, A. S. (2016). Lidar remote sensing of cloud formation caused by low-level jets. *Journal of Geophysical Research: Atmospheres*, *121*. https://doi.org/10.1002/2015JD02459

Su, J., McCormick, M. P., Wu, Y., Lee, R. B. III, Lei, L., Liu, Z., & Leavor, K. R. (2013). Cloud temperature measurement using rotational Raman lidar. *Journal of Quantitative Spectroscopy and Radiative Transfer*, *125*, 45–50.

Su, J., Zhang, Y., Hu, S., Cao, K., & Zhao, P. (2008). Raman lidar measuring tropospheric temperature profiles with many rotational Raman lines. *Spectroscopy and Spectral Analysis*, *28*, 188–190.

Vaughan, G., Wareing, D. P., Pepler, S. J., Thomas, L., & Mitev, V. (1993). Atmospheric temperature measurements made by RR scattering. *Applied Optics*, *32*, 2758–2764.

Whiteman, D. N., Melfi, S. H., & Ferrare, R. A. (1992). Raman lidar system for the measurement of water vapor and aerosols in the Earth's atmosphere. *Applied Optics*, *31*(16), 3068–3082. https://doi.org/10.1364/AO.31.003068